Advancing 2D reaction rate measurements in BNCT: Validation of the indirect neutron radiography method

Xinyu Wang [a,b], Diyun Shu [a,b,*], Changran Geng [a,**], Xiaobin Tang [a], Yuan-Hao Liu [c,b,d,a]

[a] Department of Nuclear Science and Technology, Nanjing University of Aeronautics and Astronautics, Nanjing, Jiangsu Province, 210016, P.R. China
[b] Neuboron Therapy System Ltd., Xiamen, Fujian Province, 361028, P.R. China
[c] Neuboron Medtech Ltd., Nanjing, Jiangsu Province, 211112, P.R. China
[d] BNCT Center, Xiamen Humanity Hospital, Xiamen, Fujian Province, 361006, P.R. China

A B S T R A C T

The precise characterization of neutron beams is a cornerstone of Boron Neutron Capture Therapy (BNCT). While Instrumental Neutron Activation Analysis (INAA) is the standard technique for neutron flux measurement, it is limited in its ability to capture two-dimensional (2D) reaction rate distributions. This study aims to validate the Indirect Neutron Radiography (INR) method for 2D reaction rate quantification, addressing critical variables such as temperature sensitivity and signal fading. We designed and constructed an optimized INR platform comprising an Imaging Plate (IP), readout device, activation detectors (copper foils), and real-time temperature monitoring. Comprehensive experiments were conducted to investigate the impact of ambient temperature and fading time on IP signal reliability. A robust calibration curve was formulated, linking IP signals to dose deposition metrics, thereby enabling precise reaction rate assessments. The study found that IP signals are minimally sensitive to temperature variations (less than 0.1% change per 1 °C), but are subjected to linear fading over time, necessitating stringent temperature control and time-dependent signal corrections. A mathematical relationship between IP signals and dose deposition was established, represented by $Y = 20,500 \times x^{0.01803}$-21103. Application of the INR method revealed that the depth-dependent reaction rates in copper strips closely aligned with those acquired through INAA, exhibiting a relative deviation of less than 5% within a 4cm depth range inside the phantom. Our findings demonstrate that the INR method offers a robust alternative to traditional INAA for capturing 2D reaction rates, effectively addressing complexities like temperature sensitivity and signal fading. While challenges persist, particularly in the realm of measurement errors, this study lays the groundwork for further methodological refinements and broadens the scope for future research in BNCT neutron beam characterization.

1. Introduction

Boron Neutron Capture Therapy (BNCT) is an advanced form of radiotherapy, distinguished by its utilization of heavy charged particles generated through neutron capture reactions for the targeted eradication of tumor cells. The therapeutic efficacy of BNCT is strictly dependent on the synergy combination of a neutron beam and boron-containing pharmaceutical agents (Hu et al., 2022; Wang et al., 2023). Consequently, one of the basic prerequisites for operational BNCT systems involves the precise characterization and daily quality assurance/quality control (QA/QC) of the neutron beam. These tasks are predominantly accomplished through specialized radiation measurement techniques (Liu et al., 2011).

Instrumental Neutron Activation Analysis (INAA) stands as the predominant method for neutron beam quantification in BNCT, offering capabilities for measuring both neutron intensity and spectral distribution (Liu et al., 2009a; Miller et al., 2011). Its advantages include robust exclusion of gamma-ray interference, high measurement reliability, and operational flexibility (Liu et al., 2009b). Nonetheless, conventional INAA techniques are constrained by their focus on total radioactive emissions from activation detectors, often recurring to high-purity germanium (HPGe) detectors, thereby limiting the scope to

---

point-based or one-dimensional assessments (Lin et al., 2016).

Even when INAA is adapted for two-dimensional (2D) neutron profile measurements, the limitations in resolution and operating time make it unsuitable for current applications. Addressing these shortcomings, the work by Pi-En Tsai et al. (2010) has explored the potential of Indirect Neutron Radiography (INR). The basic principle of INR is the irradiation of an activation detector by a neutron beam, resulting in the generation of radionuclides, after which a film-like detector is deployed to measure the radioactivity in the activation detector. Since the radioactivity is directly proportional to the neutron flux, the distribution of signals captured by the film-like detector can thereby provide a relative measurement of 2D neutron flux distributions.

Beyond the techniques based on neutron activation, alternative methodologies for 2D neutron profile measurement have been investigated. For instance, Seiichi Yamamoto et al. (2022) employed a hybrid system combining luminescence plates and a cooled charge-coupled device (CCD) camera to characterize 2D neutron beam patterns via the spatial distribution of fluorescent light during neutron irradiation. Similarly, G. Gambarini et al. (2010, 2011, 2015) proposed the use of gel dosimetry for measuring neutron beam doses, subsequently translating these measurements into 2D flux distributions.

In summary, existing methodologies for 2D neutron profile measurements are limited to measuring relative distributions, unlike the NAA method, which enables the measurement of absolute reaction rates — defined as the number of interactions occurring per cubic centimeter per second per atom between neutrons and activation detector nuclei. Compared to the 2D neutron profile measurements, the quantitative measurement of 2D reaction rates can not only reflect the neutron intensity but also indirectly verify the neutron beam's energy spectrum, which plays a significant role in validating the source description of BNCT neutron beam and the dose calculation of treatment planning system. If a 2D measurement technique successfully characterizes neutron beams via reaction rates, it would significantly enhance the comprehensiveness, accuracy, and efficiency of BNCT beam characterization.

The objective of this work is to further improve the INR method, addressing the challenges of applying it to 2D reaction rate measurements in BNCT, with preliminary validation of its measurement accuracy. With continued development in the future, it is anticipated that the optimized INR method will be extensively utilized for characterizing BNCT neutron beam.

2. Materials and methods

2.1. The process of optimized indirect neutron radiography (INR) method

Traditionally, the INR method utilizes the IP signal distribution to represent the 2D neutron profile, yet it fails to provide a quantitative measurement of the reaction rate distribution. The primary objective of this investigation is to refine and advance the INR method, specifically targeting its application in the absolute measurement of reaction rates. A schematic representation of the optimized INR procedure is provided in Fig. 1 (a).

In the initial phase, a large metal foil is selected to function as the activation detector. This foil is subjected to irradiation by a neutron beam, and radionuclides are generated through activation reaction. Following irradiation, the foil is meticulously positioned on an imaging plate (IP) for exposure. Radiations emitted during the decay of the radionuclides deposit dose in the IP's phosphor layer. With the term dose is intended the energy absorbed per unit of mass of IP phosphor layer. The subsequent image retrieval from the IP is facilitated using a specialized reader, and the signal values are extracted through data processing in ImageJ software (version 1.49) (Schneider et al., 2012). It should be noted that both the exposure and the signal reading processes are conducted under controlled darkroom conditions.

For the realization of accurate measurements, it is imperative to establish a robust correlation between the IP signal and the foil's reaction rate (RR_{foil}). This correlation establishment process is illustrated in Fig. 1 (b). Initially, the IP signal is converted into dose deposition metrics of the radionuclide. A calibration curve needs to be developed using radionuclides of known activity to derive this correlation. Then the specific activity of the radionuclides in the foil at the beginning of the exposure phase can be determined through Equation (1).

$$D = \sum Y_i \sigma_i \cdot \int_0^{T_0} A_0 e^{-\lambda t} dt \tag{1}$$

where, Y_i represents the branching ratios for the decay processes yielding radiation i, and i stands for different radiations, such as electrons, photons, and positrons. The coefficients σ_i signify the dose deposition for these respective radiations in the phosphor layer of the IP, and can be obtained through Monte Carlo simulations. Their units are expressed in µGy (Gy: J/kg) per particle. T_0 (unit: second) denotes the exposure time of the foil on the IP, while λ represents the radionuclide's decay constant (unit: s^{-1}). Given the known dose deposition D (unit: µGy), one can calculate the activity per unit mass of the foil (A_0) using Equation (1). Subsequently, the per-atom reaction rate can be derived.
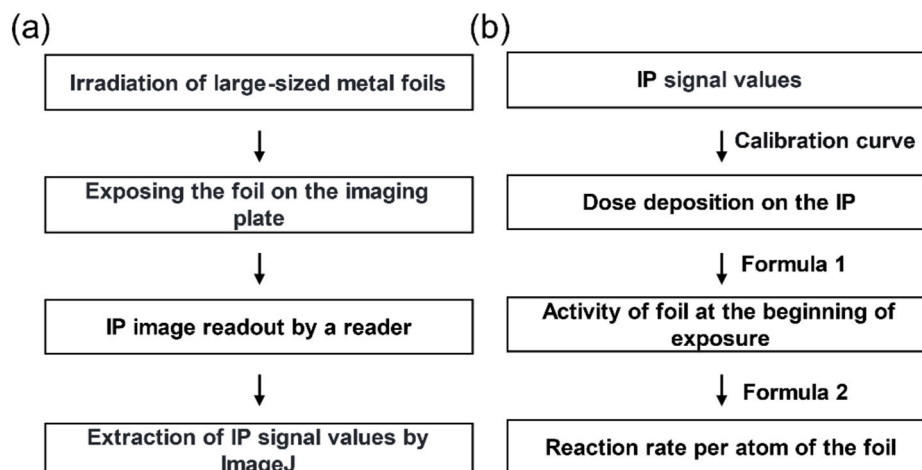

Fig. 1. Description of (**a**) the basic process of INR and (**b**) the methodology for determining RR_{foil}.

$$RR_{foil} = \frac{A_0 \cdot M}{e^{-\lambda T_a} \cdot \omega \cdot N \cdot (1 - e^{-\lambda T_i})} \qquad (2)$$

Parameters such as RR_{foil} (unit: $atom^{-1} \cdot s^{-1}$), the reaction rate per atom during the irradiation, and λ (unit: s^{-1}), the decay constant of the radionuclide, are integral to this process. Additional variables include T_a (unit: second), the cooling time interval post-irradiation but pre-IP exposure, T_i (unit: second), the irradiation time, M, the atomic mass of the activated species, N, Avogadro's constant, and ω, the mass fraction of the target element (unit: %).

2.2. Impact of temperature and fading time on IP signal

Referring to the current research on IP, it has been empirically established that IP signal quality is susceptible to fluctuations induced by temperature variations and fading of IP signal (Suzuki et al., 1997; Amemiya and Miyahara, 1988; Ohuchi et al., 2000; Tanaka et al., 2005). To ensure the reliability of the INR technique, the influence of these variables on the IP signal must be investigated. The configuration of the experimental setup is schematically presented in Fig. 2. Cobalt-60 (Co-60) and Cesium-137 (Cs-137) radioactive isotopes were positioned to administer a precise dose to the IP, thereby enabling a controlled energy deposition. Table 1 shows information about the two sources (Bhat, 1992). The IP (CR ST-VI), a product of Fujifilm, possesses dimensions of 43 cm × 35.4 cm. Signal readout from the IP is executed using a Fujifilm CR-IR 357 reader. Throughout the experimental timeline, temperature variations are meticulously monitored via a real-time thermometer (Qingping Technology, CGP23W).

In order to study the impact of temperature on the IP signal, an air conditioning system was employed to regulate the ambient temperature of the experimental setup. Both radiation sources were subjected to a 7-min exposure on a predefined region of the IP across a temperature gradient ranging from 17 °C to 27 °C, followed by an immediate signal

Table 1
Decay data of Co-60 and Cs-137.

| Radionuclide	Activity (Bq)[a]	Decay mode	Half-life	Gamma rays of decay	
				Energy (MeV)	Branch ratio (%)
Co-60	9.548×10^4	β-	1925.28 d	1.33, 1.17	99.98, 99.85
Cs-137	9.192×10^3	β-	30.08 y	0.662	85.10

[a] Activity of Co-60 and Cs-137 on April 20th, 2020.

readout. Subsequently, upon finalizing the temperature setting, the radiation sources were placed on the IP at the same position for an identical duration of exposure. Signal readouts were then conducted at varying time intervals post-exposure, specifically between 10 and 60 min, to assess the impact of fading time on the IP signal.

2.3. Calibrating curve between IP signal and dose deposition

To accurately quantify the dose deposition attributed to radionuclides via the IP signal, a well-defined calibration curve must be investigated. In this context, an array of 11 copper foils, each with a radius of 0.63 cm and a thickness of 0.021 cm, was subjected to neutron beam irradiation. To eliminate the interference from Cu-66, the copper foils need to be allowed to decay (cool) for a period after irradiation. Then the activated copper foils were strategically positioned on the IP for varying time intervals, and the ensuing signals were immediately acquired. This protocol enabled the acquisition of IP signals that correspond to a spectrum of dose depositions. It is important to note that the IP signals require adjustment to compensate for the variable influence of fading time.

The specific activity of Cu-64 in the irradiated copper foils was
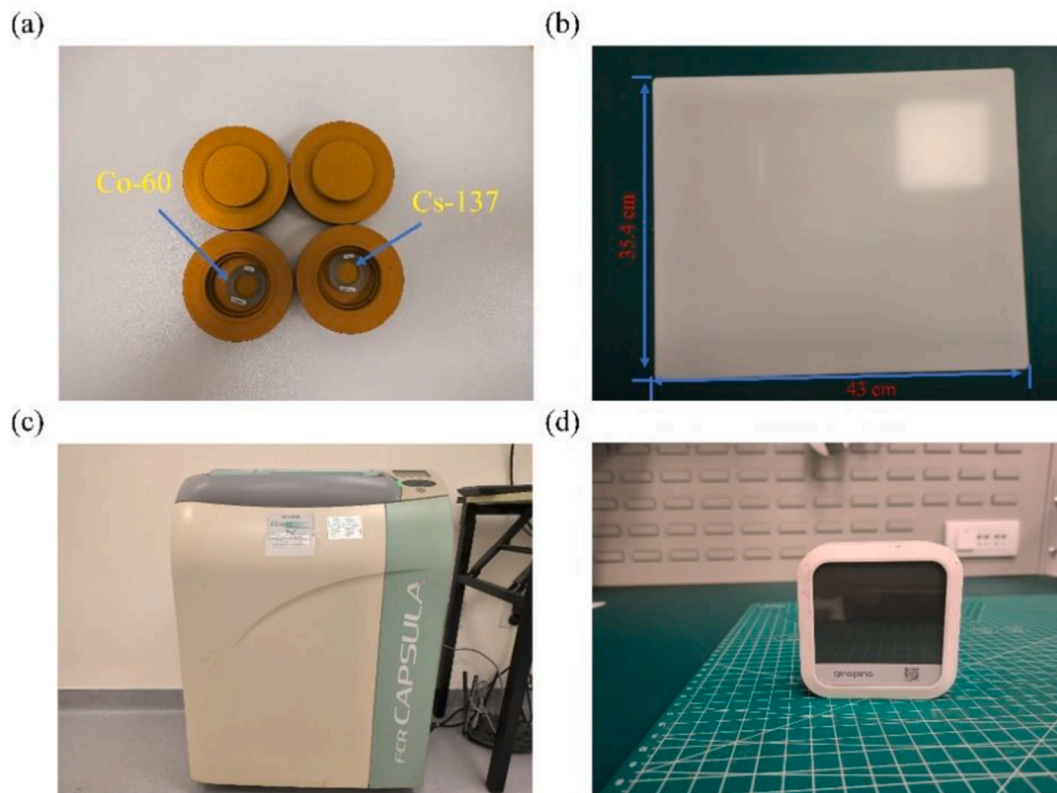
Fig. 2. Experimental setup for investigating the influence of temperature and fading time on the IP signal. (**a**) Co-60 and Cs-137 radioactive sources; (**b**) Imaging plate. (**c**) CR-IR 357 reader. (**d**) Real-time thermometer.

ascertained through spectral analysis of decay gamma-rays, utilizing a HPGe detector. Concurrently, dose deposition coefficients for Cu-64 were derived through computational simulations using the PHITS Monte Carlo code (version 3.28) (Furuta and Sato, 2021). The computational framework incorporates a copper foil with a radius of 0.63 cm and a thickness of 0.021 cm, tightly fixed to the IP (Fig. 3). Radioactivity parameters for Cu-64 were retrieved from the ENSDF database (Bhat, 1992). Various decay radiations emanating from Cu-64 were simulated to be isotropically emitted from the copper foil. The dose deposition metrics for each decay radiation on the IP were logged, as delineated in Fig. 3 (b), where the green area represent statistical region on the imaging plate. This area is consistent with the statistical region for IP signals. Subsequently, the dose deposition coefficient for each decay radiation can be obtained. Combining these data sets with Eq. (1), the model enables the calculation of dose deposition metrics for a range of exposure times.

2.4. Correction of IP signal readout

The methodology for reading the IP signal is graphically outlined in Fig. 4 (a). In this setup, a laser array excites the IP, producing a one-dimensional signal subsequently read by a detector array. This means a single laser excitation yields only a one-dimensional signal distribution along the IP, facilitating the acquisition of the 2D signal distribution across the entire IP plate via continuous scanning. During the scanning process, the direction parallel to the laser beam on the IP is referred to as the column direction, while the direction perpendicular to the laser beam is termed the row direction (as illustrated by the lighter yellow line in Fig. 4 (b)).

In previous research, it was observed that when the same dose is deposited at different positions within the same row on the IP, the readout signals are essentially the same. In contrast, depositing the same dose at various positions within the same column led to notable differences in the signals. This discrepancy can be attributed to the excitation and readout methods: positions within the same column on the IP are excited by diverse spots from the line laser, capturing the signals with distinct pixels on the detector array. Conversely, any position within the same row is excited by the same laser spot, with the signals read by the same pixel on the detector. Thus, this variance is likely attributable to the combined effects of variability in laser excitation and inconsistency in detector readout, possibly due to uneven line laser intensity or variable detection sensitivity of the detector array. To ensure the accuracy of 2D reaction rate measurements, a calibration method using an activated copper plate was developed.

Initially, as depicted in Fig. 4 (b), the activated copper plate was exposed to the IP, and the resultant signals were captured. Subsequently, the copper plate underwent a 90-degree counterclockwise rotation (see Fig. 4 (c)), followed by exposure and IP signal readout under conditions identical to the first step. Furthermore, the signals from the lighter yellow line in the first step were transmuted into a reaction rate distribution using the pre-established calibration curve and computational formula. Since the IP signals from the entire line are read by the same laser spot and same pixel of the detector array, the obtained distribution of reaction rate is correct. After rotating the copper plate by 90°, the actual distribution of the reaction rate at the position of the lighter yellow line does not change. Then, the reaction rate distribution is employed to acquire an accurate IP signal distribution under the readout conditions corresponding to point A in the second step. The IP signal deviation at the position of the lighter yellow line can be determined by subtracting the IP signal distribution measured in the second step from the deduced IP signal distribution. Due to the adoption of a line-scan readout method, the IP signal deviation in the different rows of Fig. 4 (b) is identical, thereby enabling the acquisition of a two-dimensional signal difference matrix. The measured IP signal needs to be corrected using this difference matrix.

2.5. Reaction rate distribution measurement of copper foil

For the measurement of reaction rate distribution, the dose deposition coefficients must be determined. The dose deposition coefficients described in Section 2.3 allows calculating the dose deposition in the statistical region caused by the decay radiations from the entire copper foil. In contrast, the dose deposition coefficients for reaction rate measurement are applied to correlate the dose deposited in the IP with the radionuclide activity of the relevant region on the copper foil located directly above it. To enhance the resolution of reaction rate measurement as well as to consider the influence of surrounding areas on the measurement region, the computational framework for the dose deposition coefficients was adjusted to enable a voxel-to-voxel transformation of dose deposited to activity. Based on the computational framework presented in Fig. 3, the dimensions of the copper foil have been altered to 1 cm × 1 cm × 0.02 cm, with the statistical region remaining the same. However, only the number of radiations emitted within the 0.1 cm × 0.1 cm × 0.02 cm region of the copper foil directly above the statistical region was tallied. Subsequently, the dose deposition coefficient for each decay radiation can be obtained by dividing the dose deposition by the number of radiations emitted from the corresponding region of the copper foil.
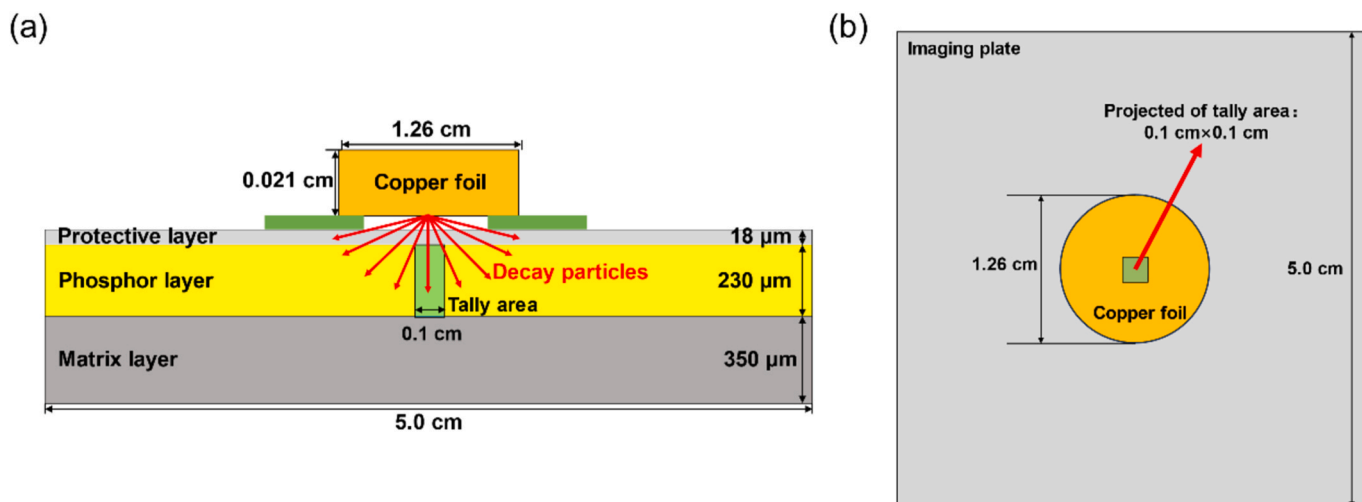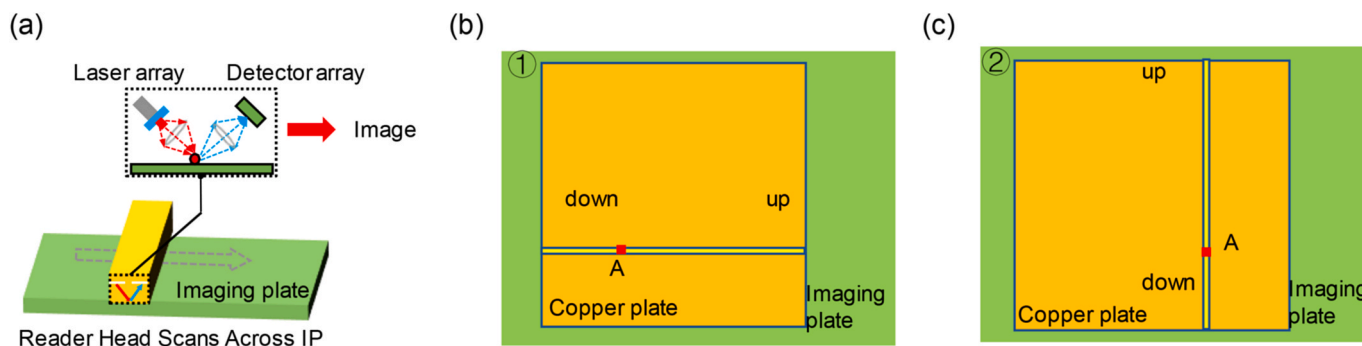

Fig. 3. Computational framework of dose deposition of Cu-64 decay radiations on the IP phosphor layer. (a) Side view of the computational model, the green area is paper tape for positioning. (b) Top view of the computational model.

Fig. 4. Methodology for reading and correction of the IP signal. (**a**) Readout process of IP signal by laser excitation (Cowen et al., 2007). (**b**) First IP signal correction step using copper plate. (**c**) Second IP signal correction step with rotating the copper plate by 90°.

The investigation of reaction rate distribution via the INR technique was conducted employing an epithermal neutron beam and a PMMA (Poly (methyl methacrylate)) phantom. The neutron beam was generated by the NeuPex Accelerator-Based Boron Neutron Capture Therapy (AB-BNCT) system, installed at Xiamen Humanity Hospital-Neuboron BNCT Center (XHH BNCT Center) and developed by Neuboron Medical Group (Dai et al., 2023). Under proton beam conditions of 2.3 MeV and 7 mA, the epithermal neutron flux at the beam exit center exceeds 5×10^8 n cm^{-2} s^{-1}. The beam exit diameter was regulated using a collimator with an opening of 12 cm in diameter. A PMMA phantom as illustrated in Fig. 5, with dimensions of 30.6 cm (L) × 30.6 cm (W) × 30.3 cm (H), was meticulously positioned at the beam exit, and its alignment was ensured via a laser positioning system. The distance between the beam exit and the PMMA phantom was minimized to zero, while simultaneously maintaining perfect axial alignment.

In this study, both copper strips and plates were utilized as activation detectors. The reaction rate distribution for copper strips ($RR_{Cu\text{-}strip}$) and plates ($RR_{Cu\text{-}plate}$) was assessed using the INR method. Specifically, a copper strip of dimensions 20 cm × 1 cm × 0.02 cm was aligned along the phantom's central axis to evaluate the depth-wise reaction rate distribution, as delineated in Fig. 5 (a). The strip was subjected to a 20-min irradiation under the aforementioned proton beam conditions, followed by a 30-min exposure on the IP, prior to signal readout. The irradiated strip was then partitioned into smaller sections of either 0.5 cm or 1 cm in length and analyzed via INAA to quantify the reaction rates. This data was then compared with INR-derived metrics to validate the method's accuracy and applicability.

To perform a 2D reaction rate assessment, a copper plate with dimensions of 30 cm × 30 cm × 0.02 was utilized. As depicted in Fig. 5 (b), the copper plate was placed perpendicular to the beam direction at a depth of 2.5 cm within the phantom. It was subjected to a 15-min irradiation followed by a 40-min exposure on the IP. The settings and

data processing methodologies remained consistent with those employed for the copper strip. Given the complexities associated with direct $RR_{Cu\text{-}plate}$ measurement via INAA, the INR method was validated by measuring $RR_{Cu\text{-}strip}$ at an equivalent depth. The specific placement of this strip is depicted in Fig. 5 (c), with neutron irradiation settings replicating those for the copper plate. Post-irradiation, the strip was segmented into 1 cm lengths, and their reaction rates were gauged using INAA. Theoretically, the reaction rates for these $RR_{Cu\text{-}strip}$ segments should coincide with those from the corresponding regions on the copper plate.

3. Results

### 3.1. Impact of temperature and fading time on IP signal

To reduce the impact of signal fading on IP readouts, measurements were conducted immediately following exposure. The robustness of this readout approach was confirmed through a series of ten consecutive tests using Co-60, each with an exposure time of 7 min at a consistent IP position. The resultant relative standard deviation for these ten measurements was a mere 0.25%, as detailed in Table 2. Consequently, this validated readout methodology was employed in all subsequent investigations. Fig. 6 graphically illustrates the IP signal's sensitivity to temperature fluctuations when generated by two different radiation sources. It is evident that the IP signal incrementally decreases as ambient temperature increases, given a constant dose deposition. Interestingly, a 1 °C shift in temperature has a relatively minimal impact on the IP signal. For example, in the context of Cs-137, the relative change in IP signal is a mere 0.1% when the temperature varies from 24 °C to 25 °C. Even so, it is crucial to maintain temperature control, ensuring that fluctuations do not exceed a 1% range during the application of the INR method.
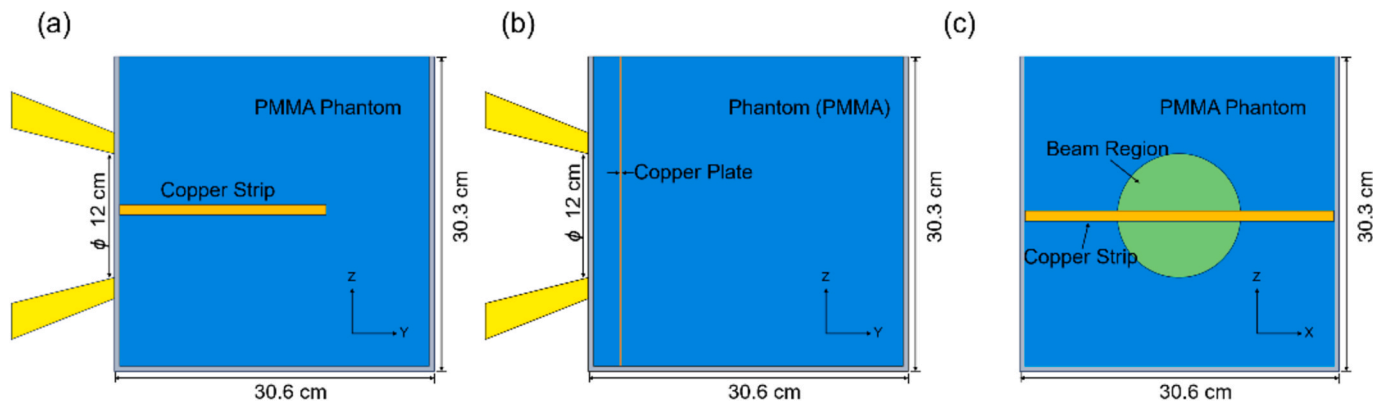
Fig. 5. Schematic diagram of copper strip and copper plate inside PMMA phantom irradiated by epithermal neutron beam. (**a**) Copper strip aligned along the phantom's central axis. (**b**) Copper plate positioned at a depth of 2.5 cm within the phantom. (**c**) Copper strip positioned at the same depth as the copper plate.

Table 2

IP signal readout immediately after 7-min exposure with Co-60 for 10 times and its relative standard deviation.

No.	1	2	3	4	5	6	7	8	9	10	RSD
Readout	2780	2790	2794	2792	2783	2792	2785	2787	2773	2778	0.25%
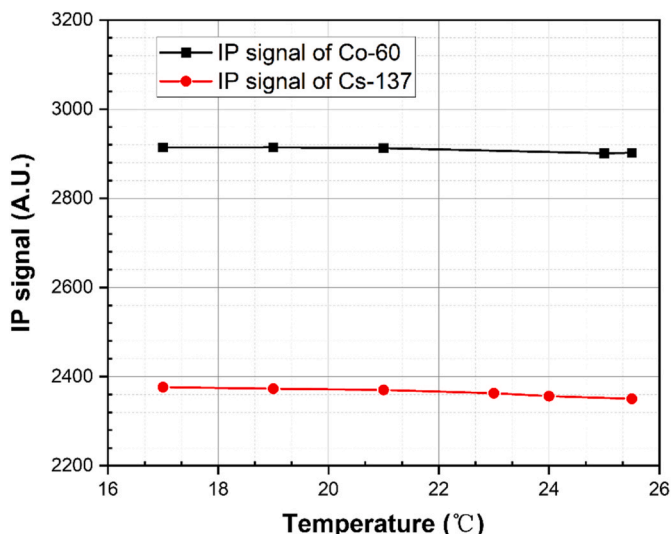
Fig. 6. Changes in IP signal generated by two different radiation sources with respect to ambient temperature variations.

Other studies have consistently maintained the ambient temperature at 25 °C, typically through an air conditioning system. Fig. 7 delineates the decline in IP signals generated by two radiation sources over varying fading times. The fading value of IP signal is obtained by subtracting the IP signal readout at varying time intervals immediately after exposure. Within a 60-min window, the decay value of the IP signal appears to be linearly positively correlated with the fading time, assuming a constant energy deposition from the radioactive source. Therefore, due to the protracted exposure times inherent in the INR method, corrections based on fading time are indispensable for the IP signal.

The relationship between IP signal attenuation and fading time, although linear, poses complex challenges for signal correction. The complexity arises because the signals generated during the exposure
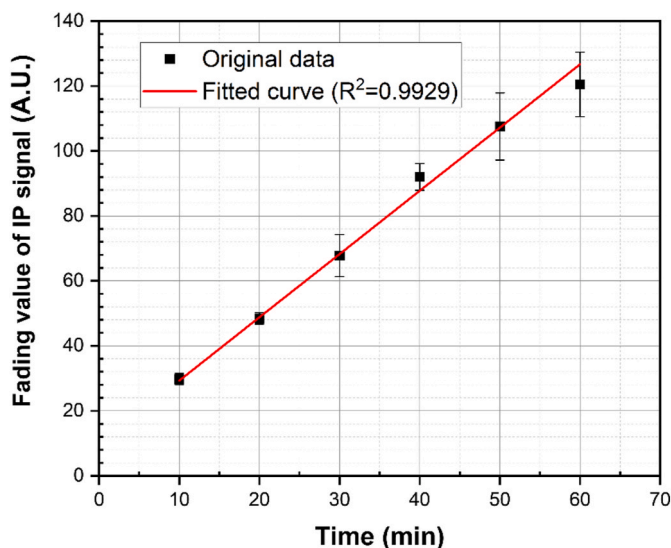
Fig. 7. Decline in IP signal generated by two different radiation sources over varying fading times.

period are different across various time periods, and the fading time of the signals produced within each time interval also varies. Consequently, fading time cannot be simply equal to exposure time. A nuanced approach is required, involving the calculation of a weighted average of fading times throughout the exposure duration.

Specifically, in the case of Cu-64 exposures, the energy deposition to IP per unit time can be considered uniform if the exposure time is substantially shorter than Cu-64's half-life. Under these conditions, the weighted average fading time approximates half of the total exposure time. The following formula is used to calculate the average fading time, t_f, as follows.

$$t_f = \sum_{t=1}^{T_0} \frac{e^{-\lambda t} \cdot (T_0 - t)}{\int_1^{T_0} e^{-\lambda t} \mathrm{d}t} \tag{3}$$

where T_0 (unit: second) is the exposure time of the foil on the IP.

3.2. Calibration curve between IP signal and dose deposition

A calibration curve was constructed using 11 copper foils. The activity of Cu-64 at the onset of the initial exposure and the dose deposition imparted to each copper foil on the IP during various exposure times are tabulated in Table 3. To achieve a measurement uncertainty below 2%, foil exposures were conducted over a protracted time span. Table 4 enumerates the dose deposition coefficients corresponding to each decay radiation of Cu-64, maintaining a calculation uncertainty consistently below 1%. Subsequently, the dose deposition for each copper foil exposure is computed, using both the activity and these dose deposition coefficients. The variance in doses at identical exposure durations can be attributed to the decay dynamics of the activated foils. Fig. 8 elucidates the relationship between IP signal and dose deposition, with each data point adjusted for fading effects. Initially, the IP signal escalates rapidly in correspondence with increasing dose deposition but eventually tapers off to a more gradual rate of increase. The empirical data has been fitted to the equation $Y = 20500 \times X^{0.01803} - 21103$, thereby a deposition dose of active radionuclides on the IP can be quickly obtained.

In the low-dose domain, a rapid increase of IP signals relative to dose deposition is observed, as shown in Fig. 8. Although the measurement error in this domain exerts a minimal influence on dose deposition

Table 3

Activity of Cu-64 at the onset of the initial exposure and the dose deposition on the IP for different subsequent exposures.

| Number	Activity (Bq)[a]	Dose deposition (µGy)			
		60 min[c]	50 min	60 min	30 min
1	70,175	2709	2003	1085	515
2	67,812	2618	1936	1048	498
3	64,805	2501	1850	1002	476
4	63,966	2469	1826	989	470
5	59,867	2311	1709	985	440
6	20,083	-[b]	573	310	147
7	19,412	749	554	300	143
8	19,326	746	552	299	142
9	18,763	736	536	290	138
10	17,966	710	513	278	132
11	15,146	643	432	234	111

[a] Activity of 11 foils at the beginning of the first exposure.
[b] There is no data here because this foil is not exposed.
[c] The time is the exposure time on the imaging plate.

Table 4
Dose deposition coefficients for calibration curve establishment.

Radiation Type	Electron	Photon	Positron	Calculation Uncertainty
Deposition coefficient (μGy/number)	1.32×10^{-5}	3.84×10^{-7}	3.36×10^{-5}	< 1%
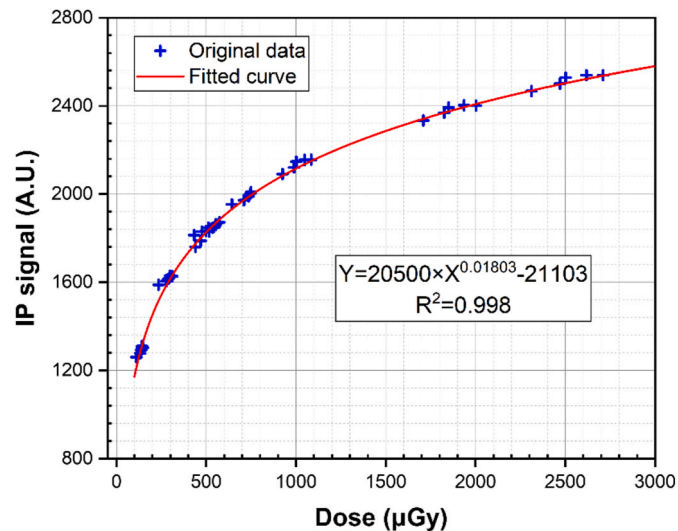
Fig. 8. Calibration curve between IP signal and dose deposition.

determination, the inherently low amplitude of IP signals introduces a relatively high margin of error. Consequently, when deploying the INR methodology, both the magnitude of IP signals and their consequential impact on dose deposition must be rigorously considered. To augment the reliability of INR, it is imperative that the signal amplitude be sufficiently robust, necessitating the deposition of an adequate dose on the imaging plate during the exposure phase.

3.3. Correction of IP signal readout

Fig. 9 (a) presents the initial IP signal image acquired from the exposure of the copper plate during the first phase of the correction process. The subsequent IP signal image, captured after rotating the copper plate, is depicted in Fig. 9 (b). Applying the correction methodology outlined in Section 2.4, the IP signals in Fig. 9 (b) were rectified, yielding the corrected image illustrated in Fig. 9 (c). In the three figures, the IP signal distribution at the location of the lighter yellow line correspond to the same exposed position on the copper plate. The one-dimensional IP signal distributions, which are derived from the lighter yellow line in these images, are collectively displayed in Fig. 9 (d).

It is important to note that the discrepancy in the IP signal's relative distribution at the position of the lighter yellow line between the two exposures is attributable to variations introduced by the machine. Nevertheless, post-correction in the second exposure mode, the distribution closely aligns with the IP signal distribution procured from the initial exposure mode. While the data matched well at the central portion of the figure, deviations were observed at edge positions. This inconsistency is likely attributable to the lack of proximity between the Cu plate and the imaging plate during the exposure phase in the peripheral regions. Importantly, the empirical framework of this study predominantly focused on uniform regions.

3.4. Reaction rate distribution measurement of copper strip

Fig. 10 (a), (b), and (c) display the original IP signal images

generated by exposing the copper strip on the IP at varying cooling intervals (T_a = 13 min, 55 min, 94 min). Notably, the 13-min cooling time yields an IP image that diverges significantly from those generated at the other two cooling intervals. Accounting for the phantom's wall thickness of 0.3 cm, the copper strip data commences from this point. The IP signals were subsequently transmuted into reaction rates based on the calibration curve, dose deposition coefficients (as shown in Table 5), and the formulas. A comparative evaluation was performed alongside results garnered from the INAA method, as illustrated in Fig. 10 (d) and (e).

In Fig. 10 (a), (b), and (c), peripheral signal values are discernible beyond the exposure region, a feature ascribed to the isotropic radio-active emission emanating from the Cu strip itself. Fig. 10 (g) and (h) present signal distributions that correspond to Fig. 10 (c), delineating the peak signal values across both horizontal profiles and depth directions. The IP signal generated by the Cu strip beyond the exposure zone diminishes precipitously. However, this local impact pervades all surrounding pixels. The effect is more severe compared to areas where neighboring regions exhibit similar activities. To mitigate the effects of this neighboring contribution, the present study employed a readout segment considerably larger than a single pixel.

For the copper strip subjected to a 13-min cooling period, the $RR_{Cu\text{-}strip}$ values ascertained via the INR method substantially exceeded those obtained through the INAA method. This discrepancy primarily originates from the concurrent IP signal generation by both Cu-64 (half-life = 12.7 h) and Cu-66 (half-life = 5.12 min) during the abbreviated cooling period of the Cu strip (Lipson et al., 2004). In INAA, Cu-64 and Cu-66 can be distinguished by different energy peaks of decay radiation. However, Cu-66 can only be excluded by a longer cooling time for the INR method. Conversely, for the copper strips cooled for 55 and 94 min, the outcomes from both the INR and INAA methods displayed relative congruence, manifesting a relative deviation of less than 5% within a 4 cm depth range, as shown in Fig. 10 (f).

Fig. 11 (a) showcases the outcomes of normalizing reaction rates at disparate depths to the peak reaction rate. Owing to the proportional activity relationship between Cu-66 and Cu-64, a consistent relative distribution of reaction rates was observed for Cu strips across varied cooling times (Fig. 11 (a)). Across all three INR measurements, the zenith of $RR_{Cu\text{-}strip}$ values consistently emerged at depths ranging from 2.3 cm to 2.8 cm. This depth range concurs with the peak $RR_{Cu\text{-}strip}$ values as indicated by the INAA method. The relative deviation in the normalized distribution of $RR_{Cu\text{-}strip}$ between the two methods remains below 5% within a 3 cm depth range, as depicted in Fig. 11 (b). Notably, within the more specific depth interval of 1 cm–3.5 cm, this deviation is further reduced to less than 2%.

Based on the findings of this section, it is crucial to ensure that the dose deposited on the IP for INR measurement is caused either by a single radionuclide or by quantifiably proportional contributions from multiple radionuclides. By managing the cooling period to ensure only a single radionuclide remains, an activation detector that initially produces a range of radionuclides can nonetheless be utilized for the INR method.

3.5. Reaction rate distribution measurement of copper plate

Fig. 12 (a) displays the original IP signal image generated by the activated copper plate. The IP signals in the image have been subjected to both readout and fading time corrections. Significantly, the image demonstrates signal loss due to poor contact between the Copper Plate and IP, as highlighted by the red circle in Fig. 12. This underscores the necessity for a tight fit between the activation detector and IP throughout the exposure process. Utilizing the INR method, a 2D distribution map of $RR_{Cu\text{-}plate}$ is constructed using the calibration curve obtained in Section 3.2, as depicted in Fig. 12 (b). To scrutinize the precision of the INR method, the reaction rates along the horizontal central axis (indicated by the red line in Fig. 12 (b)) were extracted. Concurrently, reaction rates for the copper strip, as portrayed in Fig. 5
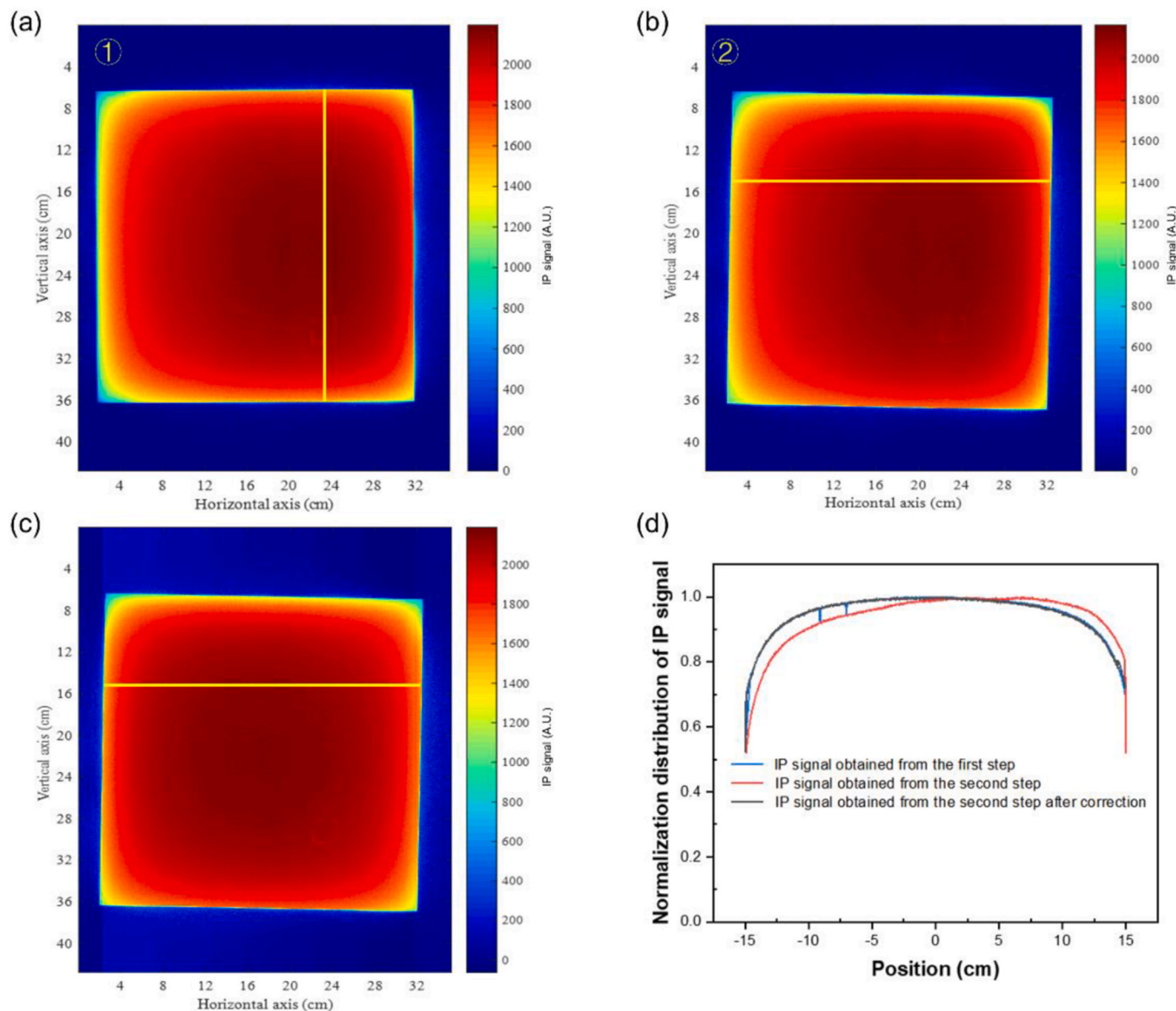
Fig. 9. IP signal images and the one-dimensional distributions at the location of the lighter yellow line acquired from the exposure of the copper plate. (**a**) IP signal image obtained from the first phase of the correction process. (**b**) IP signal image captured after rotating the copper plate. (**c**) Correction image of (**b**). (**d**) One-dimensional normalized distributions of IP signal at the location of the lighter yellow line derived from the above images.

(c), were quantified via the INAA method. A comparative analysis of reaction rates at identical positions, as measured by both methodologies, is presented in Fig. 13.

The data reveals that proximal positions to the beam's central axis yield smaller relative deviations between the INR and INAA methods. Conversely, the reaction rates determined by the two methods exhibit larger relative deviations in positions that are further away from the beam central axis. A convergence of factors contributes to these disparities, with the primary source of errors associated with INR being IP signal inaccuracies. It is worth noting that the presence of smaller IP signals consistently leads to an increase in measurement uncertainties. In addition, a misalignment or loose fit between the activation detector and the IP can further increase these errors, highlighting the more pronounced relative deviation in reaction rates at depths between 0.3 and 0.8 cm in the Cu strip, as depicted in Fig. 10 (f). To mitigate this issue, future studies will employ thicker materials. Simultaneously, consideration should be given to prolonging neutron irradiation or sample exposure times to reduce these inaccuracies.

4. Conclusion

In the endeavor to optimize BNCT, precise and comprehensive neutron beam characterization is paramount. Traditional methods such as INAA provide reliable but limited applications, particularly in measuring 2D neutron profiles. Addressing this critical gap, the present study successfully validates and advances the INR method as a viable tool for 2D reaction rate measurements in BNCT applications.

The study commenced by meticulously optimizing various parameters that influence the quality of the IP signal, such as ambient temperature and signal fading over time. Through rigorous temperature control and scientifically grounded corrections for signal decay, the INR method exhibited a robust capability for accurate reaction rate measurements. A calibrated curve was established to correlate IP signals with dose deposition metrics, further strengthening the method's reliability.

Comparative analyses conducted between INR and INAA methods for both copper strips and plates irradiated in a PMMA phantom substantiated the efficacy of INR. The results indicated remarkable congruence
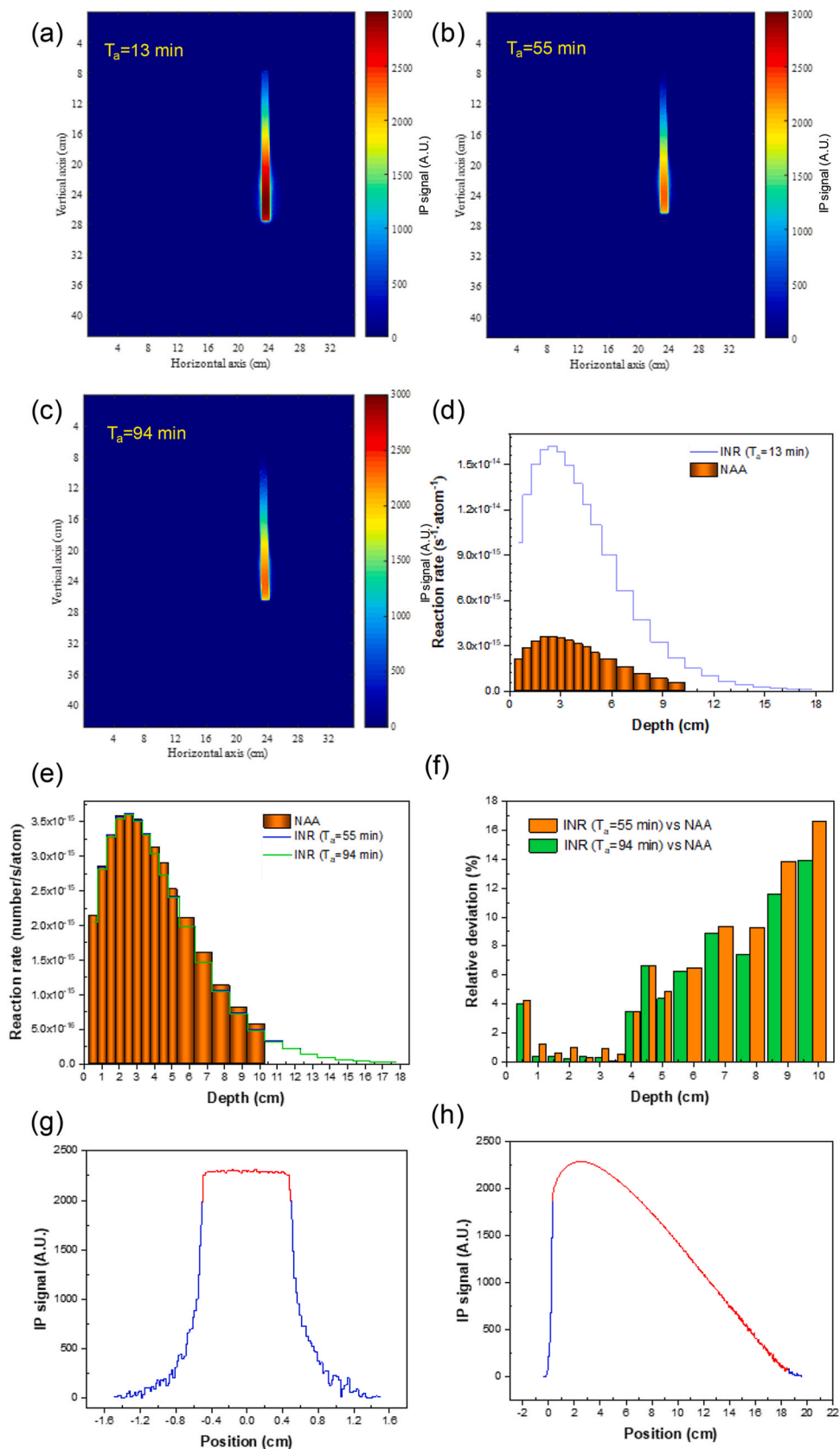
Fig. 10. Measurement of $RR_{Cu\text{-}strip}$ with INR and NAA methods. (**a-c**) Original IP signal images generated by exposing the copper strip on the IP at varying cooling intervals. (**d-e**) $RR_{Cu\text{-}strip}$ obtained by INR method compared with the NAA method. (**f**) Relative deviation between the results obtained by the two methods. (**g**) Horizontal distribution of IP signal at the location of maximum IP signal and (**h**) depth distribution of IP signal acquired from the exposure of the copper strip. The red line represents the IP signals within the exposure range of the copper strip, while the blue line represents the IP signals outside the copper strip.

Table 5
Dose deposition coefficients for reaction rate distribution measurement.

Radiation Type	Electron	Photon	Positron	Calculation Uncertainty
Deposition coefficient (μGy/ number)	1.64×10^{-3}	4.82×10^{-5}	4.21×10^{-3}	< 1%

between the two methods, especially when corrective measures for potential interference from Cu-66 were implemented. This validation affirms the INR method as a highly promising avenue for advancing 2D reaction rate measurements in BNCT.

This research has now been applied to QA/QC of neutron beams and other experiments. Despite these advancements, challenges related to measurement errors and IP signal inaccuracies persist. Future research endeavors should aim to further refine the INR method, possibly through the extension of neutron irradiation or sample exposure times, to achieve higher degrees of precision and reliability. The investigation and optimization of the neighboring effect represents another critical avenue for future research.

Broadly, the study leveraged Cu as the principal material but holds potential for adaptation to other metallic substances. Despite its efficacy in rapid 2D neutron beam plane measurement, the technique is not devoid of limitations. A significant constraint is the indiscriminate deposition of all radioactive species on the IP, introducing the potential for isotopic impurity interference. This necessitates scrupulous material selection for experiments. To assure measurement fidelity, adequate
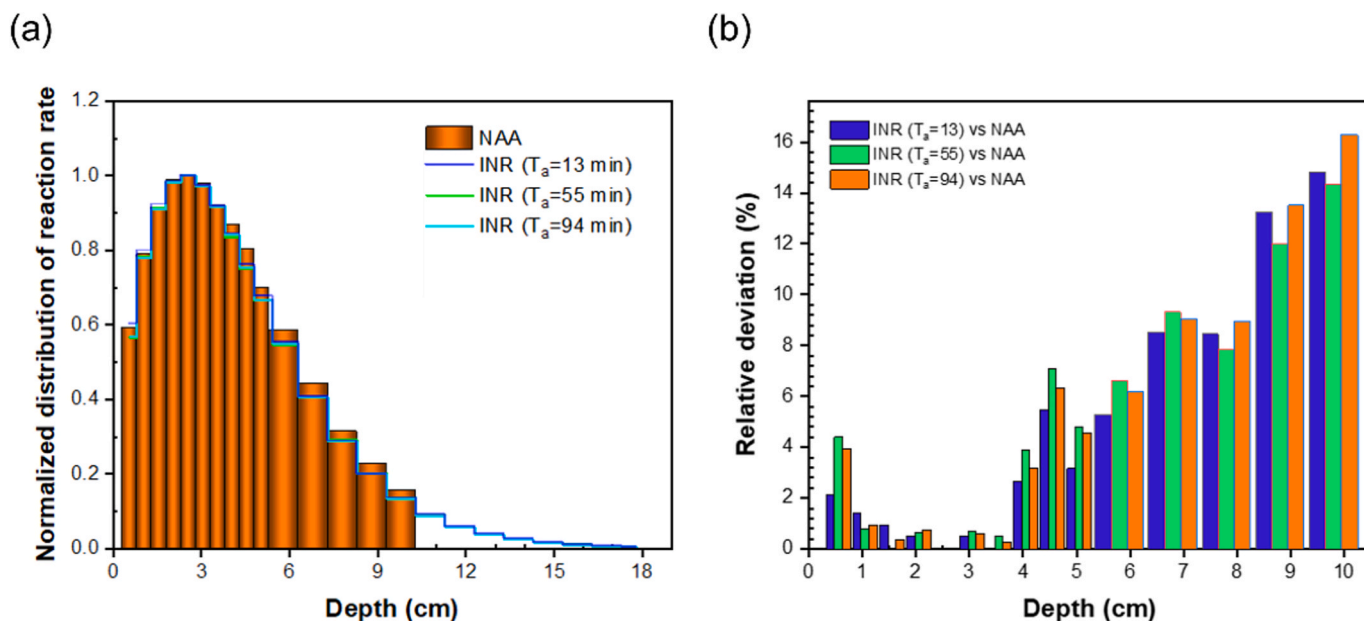

Fig. 11. (**a**) Relative distribution and (**b**) relative deviation of $RR_{\text{Cu-strip}}$ measured by INR and NAA methods.
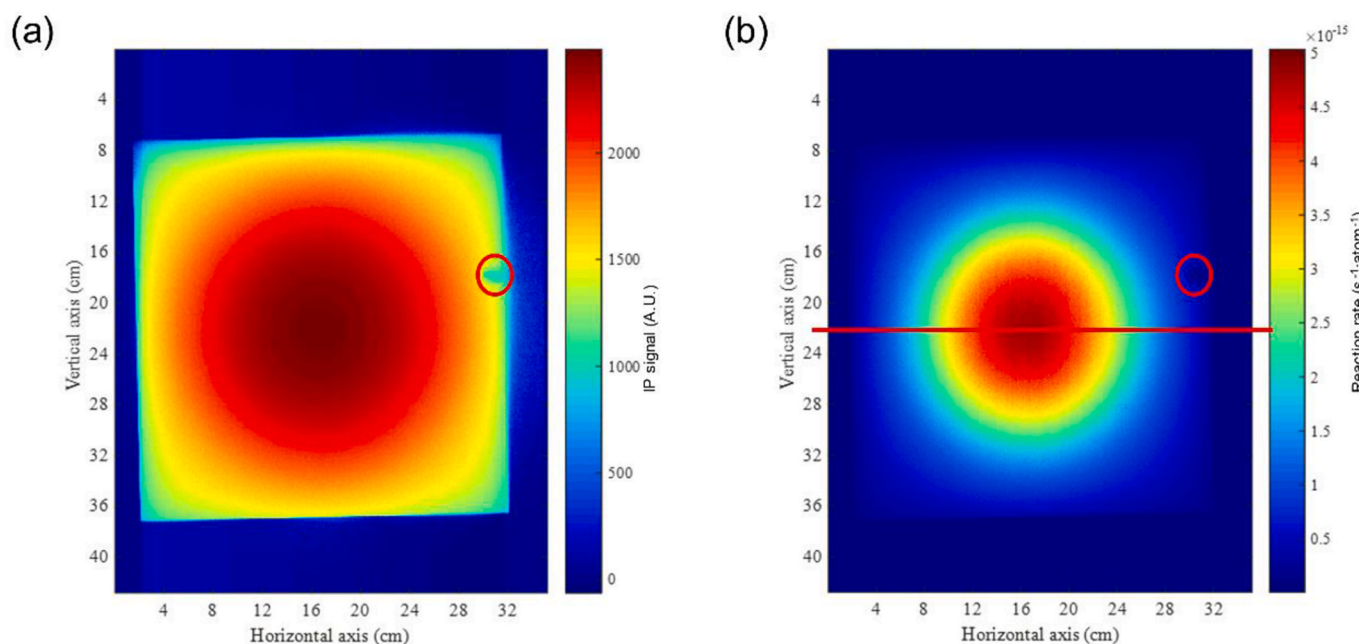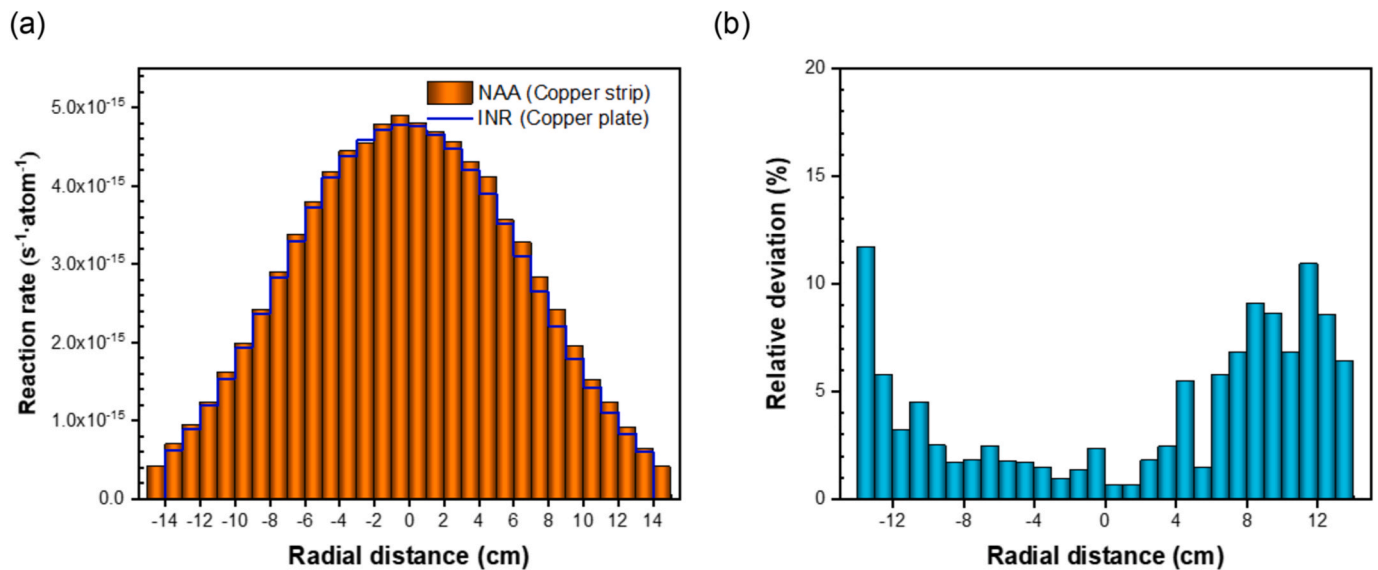

Fig. 12. (**a**) Original IP signal image and (**b**) two-dimensional distribution map of $RR_{\text{Cu-plate}}$ generated by the activated copper plate.

(a)

(b)

Fig. 13. Comparison between $RR_{\text{Cu-plate}}$ along the horizontal central axis of copper plate measured by INR method and $RR_{\text{Cu-strip}}$ obtained by a copper strip located at identical positions inside the phantom with NAA method. (**a**) One-dimensional distribution of reaction rate along the horizontal central axis. (**b**) Relative deviation of reaction rate measured by the two methods.

doses must be deposited on the IP, achievable via calibrated exposure or irradiation durations. Meticulous optimization of these parameters is indispensable for securing reliable and precise outcomes.

In summary, this study serves as a foundational framework for employing INR in BNCT, successfully adressing the intricate challenges associated with 2D reaction rate measurements. It presents INR not merely as an alternative but as an advanced methodology that complements and potentially surpasses traditional INAA, heralding a new stage in BNCT neutron beam characterization.

CRediT authorship contribution statement

Xinyu Wang: Writing – original draft, Visualization, Validation, Methodology, Investigation, Formal analysis, Data curation. **Diyun Shu:** Writing – review & editing, Supervision, Methodology, Formal analysis, Conceptualization. **Changran Geng:** Writing – review & editing, Supervision, Methodology. **Xiaobin Tang:** Writing – review & editing, Supervision. **Yuan-Hao Liu:** Writing – review & editing, Supervision, Methodology, Investigation, Formal analysis, Conceptualization.

Declaration of competing interest

The authors declare that they have no known competing financial interests or personal relationships that could have appeared to influence the work reported in this paper.

Data availability

Data will be made available on request.

References

Amemiya, Y., Miyahara, J., 1988. Imaging plate illuminates many fields. Nature 336 (6194), 89–90. https://doi.org/10.1038/336089a0.

Bhat, 1992. Evaluated Nuclear Structure Data File (ENSDF), Data Extracted Using the NNDC On-Line 339 Data Service from the ENSDF Database, File Revised as of November 12, 2021.

Cowen, A.R., Davies, A.G., Kengyelics, S.M., 2007. Advances in computed radiography systems and their physical imaging characteristics. Clin. Radiol. 62 (12), 1132–1141. https://doi.org/10.1016/j.crad.2007.07.009.

Dai, L., Liu, J., Zhao, X., Li, Y., Zhou, S., Yuan, L., Shu, D., Pan, L., Qian, Z., 2023. BPA-Containing polydopamine nanoparticles for boron neutron capture therapy in a U87 glioma orthotopic model. Adv. Funct. Mater., 2214145 https://doi.org/10.1002/adfm.202214145.

Furuta, T., Sato, T., 2021. Medical application of particle and heavy ion transport code system PHITS. Radiol. Phys. Technol. 14 (3), 215–225. https://doi.org/10.1007/s12194-021-00628-0.

Gambarini, G., Bartesaghi, G., Burian, J., Carrara, M., Marek, M., Negri, A., Pirola, L., Viererbl, L., 2010. Fast-neutron dose evaluation in BNCT with Fricke gel layer detectors. Radiat. Meas. 45 (10), 1398–1401. https://doi.org/10.1016/j.radmeas.2010.05.004.

Gambarini, G., Bartesaghi, G., Carrara, M., Negri, A., Paganini, L., Vanossi, E., Burian, J., Marek, M., Viererbl, L., Klupak, V., 2011. Imaging of gamma and neutron dose distributions at LVR-15 epithermal beam by means of FGLDs. Appl. Radiat. Isot. 69 (12), 1911–1914. https://doi.org/10.1016/j.apradiso.2011.03.017.

Gambarini, G., Artuso, E., Giove, D., Felisi, M., Volpe, L., Barcaglioni, L., Agosteo, S., Garlati, L., Pola, A., Klupak, V., 2015. Study of suitability of Fricke-gel-layer dosimeters for in-air measurements to characterise epithermal/thermal neutron beams for NCT. Appl. Radiat. Isot. 106, 145–150. https://doi.org/10.1016/j.apradiso.2015.07.036.

Hu, N., Tanaka, H., Ono, K., 2022. Design of a filtration system to improve the dose distribution of an accelerator-based neutron capture therapy system. Med. Phys. 49 (10), 6609–6621. https://doi.org/10.1002/mp.15864.

Lin, H.-X., Chen, W.-L., Liu, Y.-H., Sheu, R.-J., 2016. Characteristics and application of spherical-type activation detectors in neutron spectrum measurements at a boron neutron capture therapy (BNCT) facility. Nucl. Instrum. Methods Phys. Res. Sect. A Accel. Spectrom. Detect. Assoc. Equip. 811, 94–99. https://doi.org/10.1016/j.nima.2015.12.029.

Lipson, A.G., Miley, G.H., Kuznetsov, V.A., 2004. Anomalous neutron activation and plastic deformation of a copper cathode during electrolysis in an ultraweak thermalized neutron field. Radiat. Phys. Chem. 69 (1), 7–15. https://doi.org/10.1016/S0969-806X(03)00459-6.

Liu, Y.-H., Nievaart, S., Tsai, P.-E., Liu, H.-M., Moss, R., Jiang, S.-H., 2009a. Coarse-scaling adjustment of fine-group neutron spectra for epithermal neutron beams in BNCT using multiple activation detectors. Nucl. Instrum. Methods Phys. Res. Sect. A Accel. Spectrom. Detect. Assoc. Equip. 598 (3), 764–773. https://doi.org/10.1016/j.nima.2008.09.039.

Liu, Y.-H., Nievaart, S., Tsai, P.-E., Liu, H.-M., Moss, R., Jiang, S.-H., 2009b. Neutron spectra measurement and comparison of the HFR and THOR BNCT beams. Appl. Radiat. Isot. 67 (7–8), S137–S140. https://doi.org/10.1016/j.apradiso.2009.03.088.

Liu, Y.-H., Tsai, P.-E., Lin, Y.-C., Huang, C.-K., Liu, H.-M., Jiang, S.-H., 2011. Quality control and quality assurance procedures at the THOR BNCT facility. Appl. Radiat. Isot. 69 (12), 1897–1900. https://doi.org/10.1016/j.apradiso.2011.03.012.

Miller, M.E., Sztejnberg, M.L., González, S.J., Thorp, S.I., Longhino, J.M., Estryk, G., 2011. Rhodium self-powered neutron detector as a suitable on-line thermal neutron flux monitor in BNCT treatments. Med. Phys. 38 (12), 6502–6512. https://doi.org/10.1118/1.3660204.

Ohuchi, H., Yamadera, A., Nakamura, T., 2000. Functional equation for the fading correction of imaging plates. Nucl. Instrum. Methods Phys. Res. Sect. A Accel. Spectrom. Detect. Assoc. Equip. 450 (2–3), 343–352. https://doi.org/10.1016/S0168-9002(00)00300-4.

Schneider, C.A., Rasband, W.S., Eliceiri, K.W., 2012. NIH Image to ImageJ: 25 years of image analysis. Nat. Methods 9 (7), 671–675. https://doi.org/10.1038/nmeth.2089.

Suzuki, T., Mori, C., Yanagida, K., Uritani, A., Miyahara, H., Yoshida, M., Takahashi, F., 1997. Characteristics and correction of the fading of imaging plate. J. Nucl. Sci. Technol. 34 (5), 461–465. https://doi.org/10.1080/18811248.1997.9733692.

Tanaka, K.A., Yabuuchi, T., Sato, T., Kodama, R., Kitagawa, Y., Takahashi, T., Ikeda, T., Haonda, Y., Okuda, S., 2005. Calibration of imaging plate for high energy electron spectrometer. Rev. Sci. Instrum. 76 (1) https://doi.org/10.1063/1.1824371.

Tsai, P.-E., Liu, Y.-H., Liu, H.-M., Jiang, S.-H., 2010. Characterization of a BNCT beam using neutron activation and indirect neutron radiography. Radiat. Meas. 45 (10), 1167–1170. https://doi.org/10.1016/j.radmeas.2010.07.008.

Wang, S., Wang, N., Sheng, L., Wang, J., Song, B., Li, F., Min, X., 2023. Deciphering the potential influence of BNCT on gene expression in normal cells through bioinformatic analysis of the α-particles-induced transcriptome data. Journal of Radiation Research and Applied Sciences 16 (4), 100736. https://doi.org/10.1016/j.jrras.2023.100736.

Yamamoto, S., Yabe, T., Hu, N., Kanai, Y., Tanaka, H., Ono, K., 2022. Optical imaging of lithium-containing zinc sulfate plate in water during irradiation of neutrons from boron neutron capture therapy (BNCT) system. Med. Phys. 49 (3), 1822–1830. https://doi.org/10.1002/mp.15424.